nature chemistry

SUPPLEMENTARY INFORMATION

https://doi.org/10.1038/s41557-019-0312-z

In the format provided by the authors and unedited.

Formation of carbon–nitrogen bonds in carbon monoxide electrolysis

Matthew Jouny[1,6], Jing-Jing Lv[1,2,6], Tao Cheng[3,4,5,6], Byung Hee Ko[1], Jun-Jie Zhu[2], William A. Goddard III[3,4]* and Feng Jiao[1]*

[1]Center for Catalytic Science and Technology, Department of Chemical and Biomolecular Engineering, University of Delaware, Newark, DE, USA. [2]State Key Laboratory of Analytical Chemistry for Life Science, School of Chemistry and Chemical Engineering, Nanjing University, Nanjing, China. [3]Joint Center for Artificial Photosynthesis, California Institute of Technology, Pasadena, CA, USA. [4]Materials and Process Simulation Center, California Institute of Technology, Pasadena, CA, USA. [5]Institute of Functional Nano & Soft Materials, Jiangsu Key Laboratory for Carbon-based Functional Materials & Devices, Joint International Research Laboratory of Carbon-based Functional Materials and Devices, Soochow University, Suzhou, Jiangsu, China. [6]These authors contributed equally: Matthew Jouny, Jing-Jing Lv, Tao Cheng. *e-mail: wag@caltech.edu; jiao@udel.edu

Supplementary Information

Formation of carbon-nitrogen bonds in carbon monoxide electrolysis

Matthew Jouny,[1,†] Jing-Jing Lv,[1,2,†] Tao Cheng,[3,4,†] Byung Hee Ko,[1] Jun-Jie Zhu,[2] William A. Goddard III,[*,3,4] and Feng Jiao[*,1]

[1] Center for Catalytic Science and Technology, Department of Chemical and Biomolecular Engineering, University of Delaware, Newark, DE, 19716 (USA)

[2] State Key Laboratory of Analytical Chemistry for Life Science, School of Chemistry and Chemical Engineering, Nanjing University, Nanjing, 210093 (P. R. China)

[3] Joint Center for Artificial Photosynthesis, California Institute of Technology, Pasadena, CA, 91125 (USA)

[4] Materials and Process Simulation Center (MC139-74), California Institute of Technology, Pasadena, CA, 91125 (USA)

[5] Institute of Functional Nano & Soft Materials (FUNSOM), Jiangsu Key Laboratory for Carbon-Based Functional Materials & Devices, Joint International Research Laboratory of Carbon-Based Functional Materials and Devices, Soochow University, 199 Renai Road, Suzhou, 215123, Jiangsu, PR China

†These authors contributed equally to this work.

*Correspondence to: wag@caltech.edu (ORCID: 0000-0003-0097-5716) & jiao@udel.edu (ORCID: 0000-0002-3335-3203)

Table of Contents

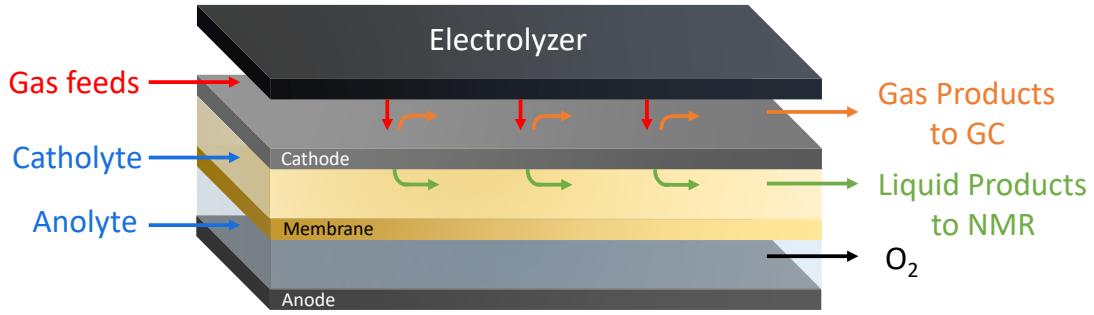

Supplementary Figure 1: Schematic of a three-compartment electrolyzer flow cell set-up.

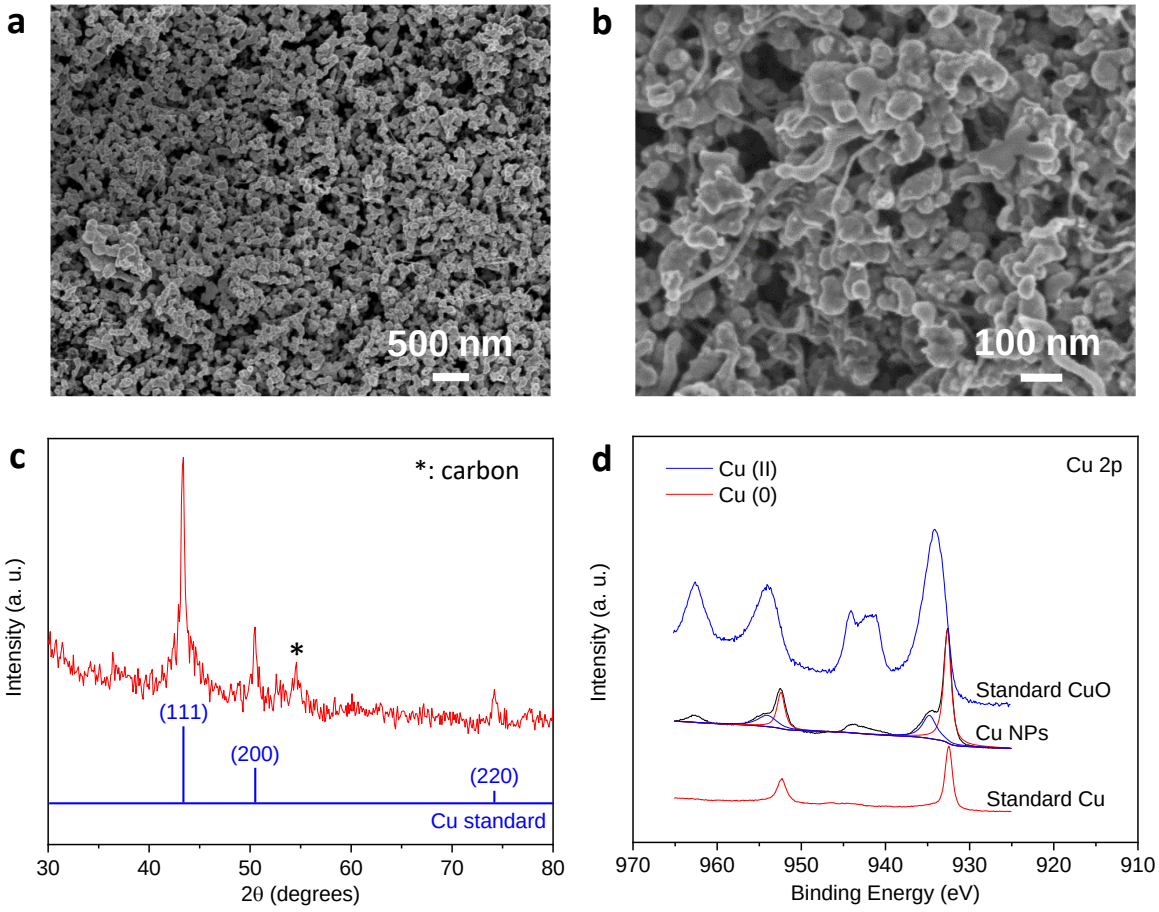

Supplementary Figure 2: Characterization of commercial Cu nanoparticles. a-b, Scanning electron microscopy images of Cu nanoparticles on the gas diffusion layer. **c,** Powder X-ray diffraction spectrum. **d,** X-ray photoelectron spectroscopy spectra.

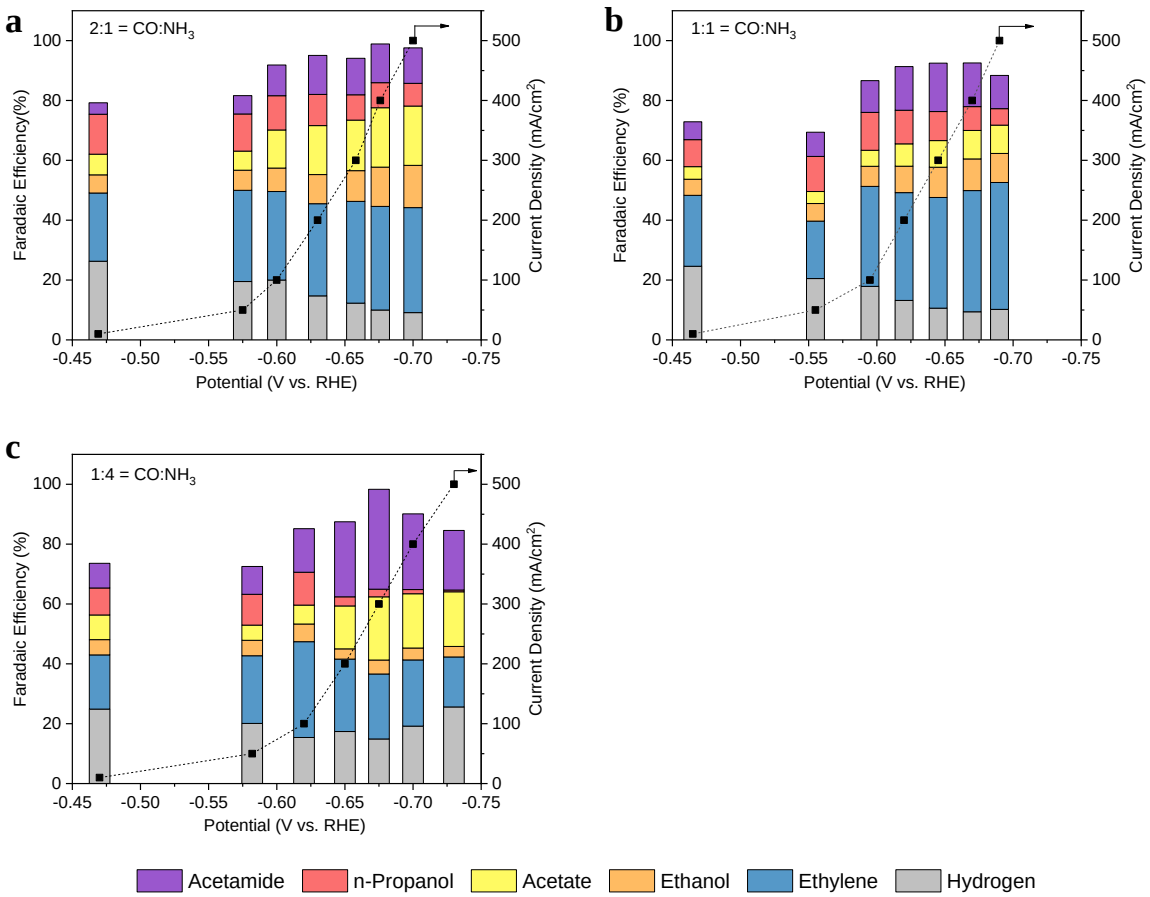

Supplementary Figure 3: Electrolysis performance for different CO/NH_3 feed ratios in 1M KOH. **a,** 2:1 (mol/mol) $CO:NH_3$ **b,** 1:1 (mol/mol) $CO:NH_3$ **c,** 1:4 (mol/mol) $CO:NH_3$

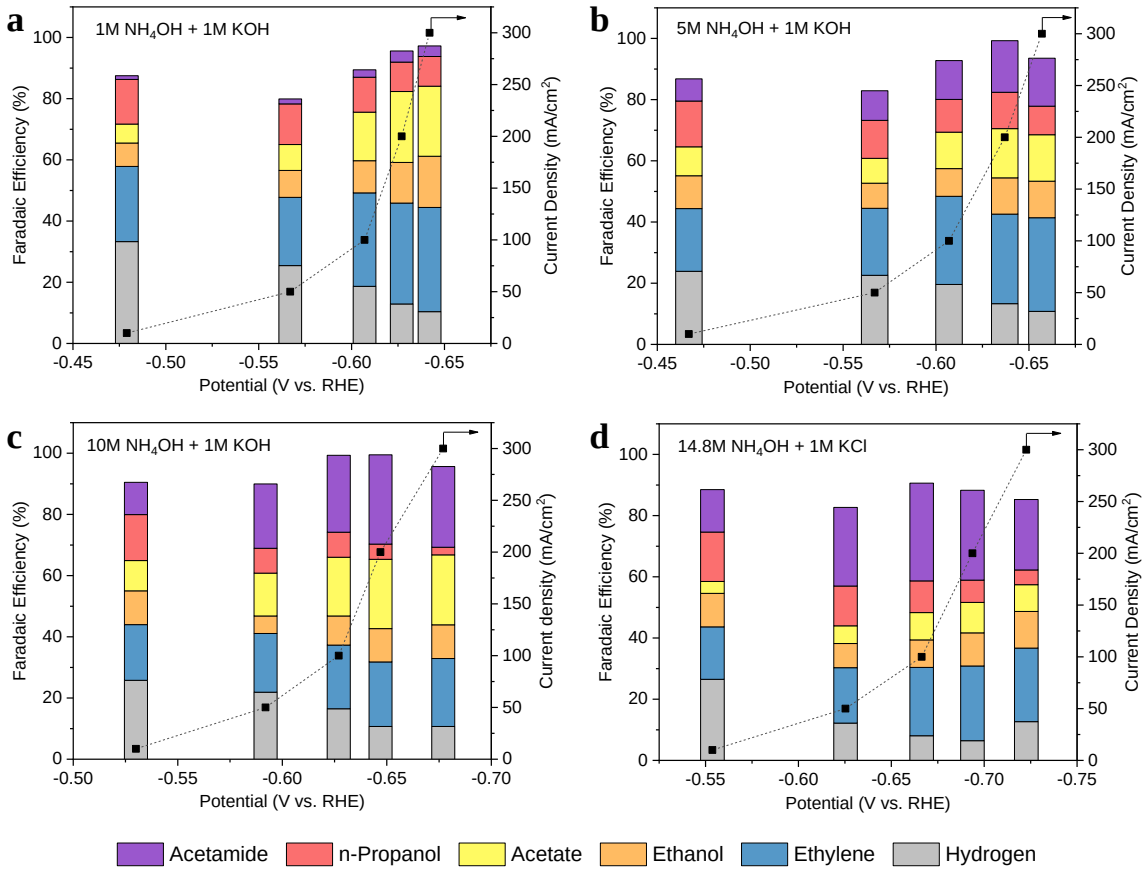

Supplementary Figure 4: CO Reduction in ammonium hydroxide electrolytes. a, 1M NH_4OH with 1M KOH. **b,** 5M NH_4OH with 1M KOH. **c,** 10M NH_4OH with 1M KOH. **d,** 14.8M NH_4OH with 1M KCl.

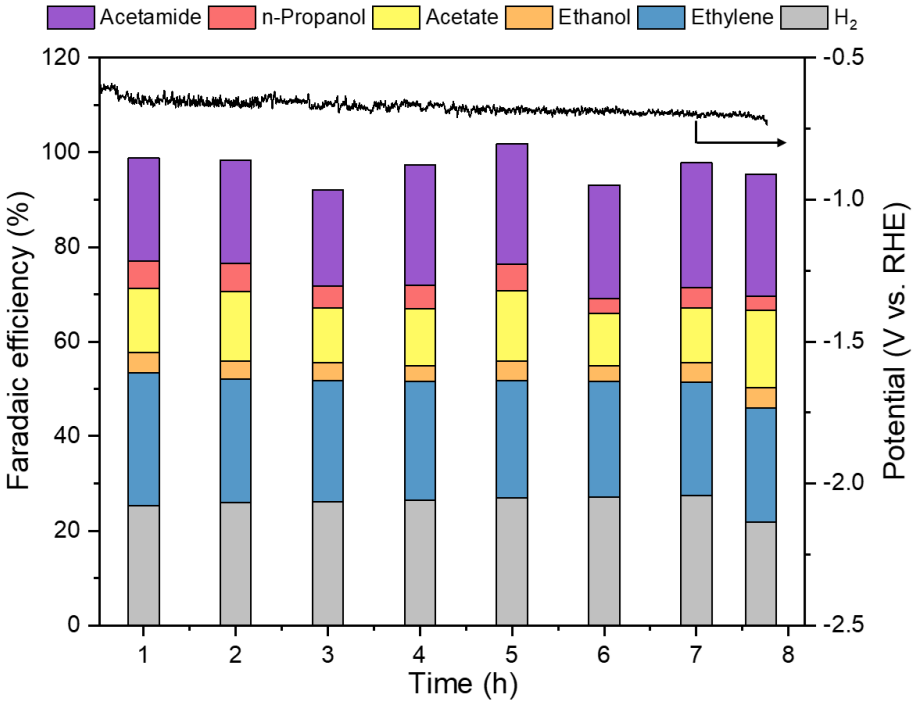

Supplementary Figure 5: Demonstration of 8-hour stability for CO electrolysis with 2:1 (mol/mol) NH_3:CO in 1M KOH at 100 mA/cm^2.

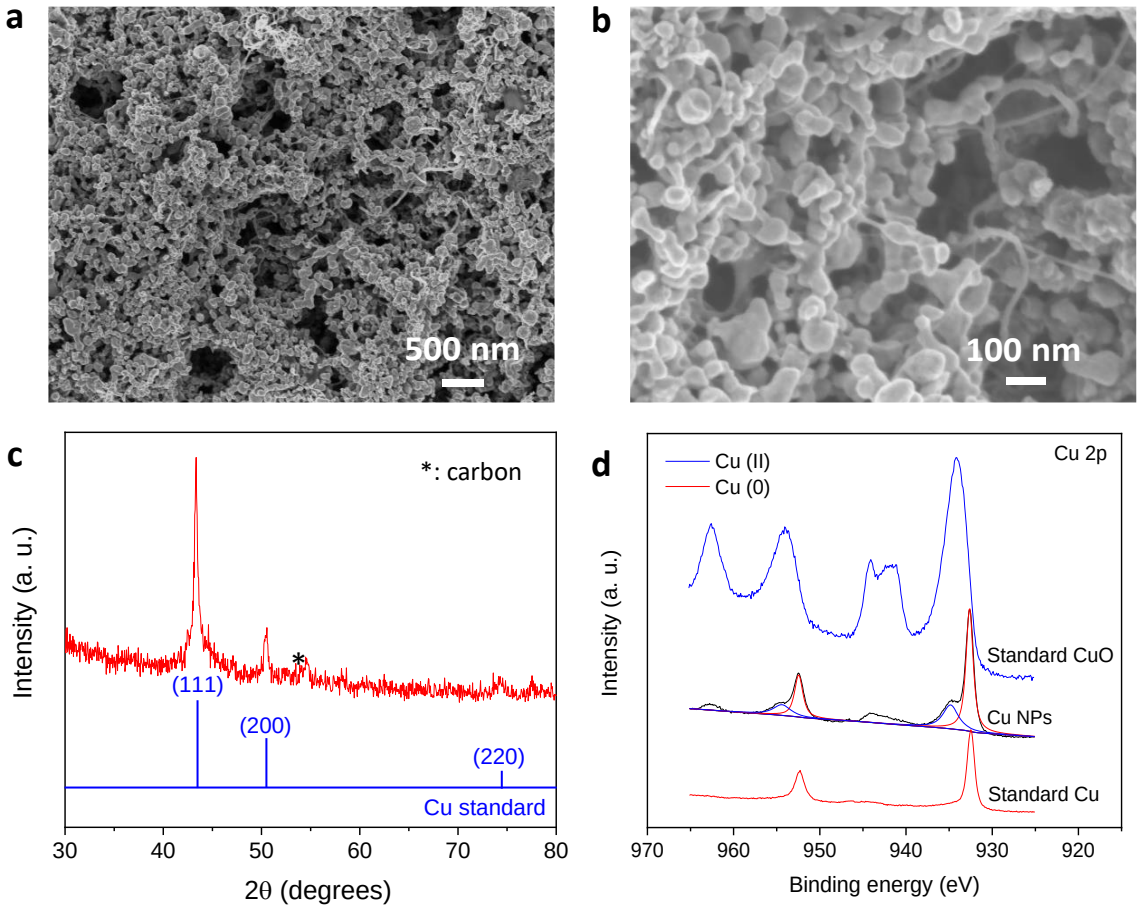

Supplementary Figure 6: Post-reaction characterization of Cu nanoparticles. a-b, Scanning electron microscopy images of Cu nanoparticles on the gas diffusion layer. **c,** X-ray diffraction spectrum. **d,** X-ray photoelectron spectroscopy spectra.

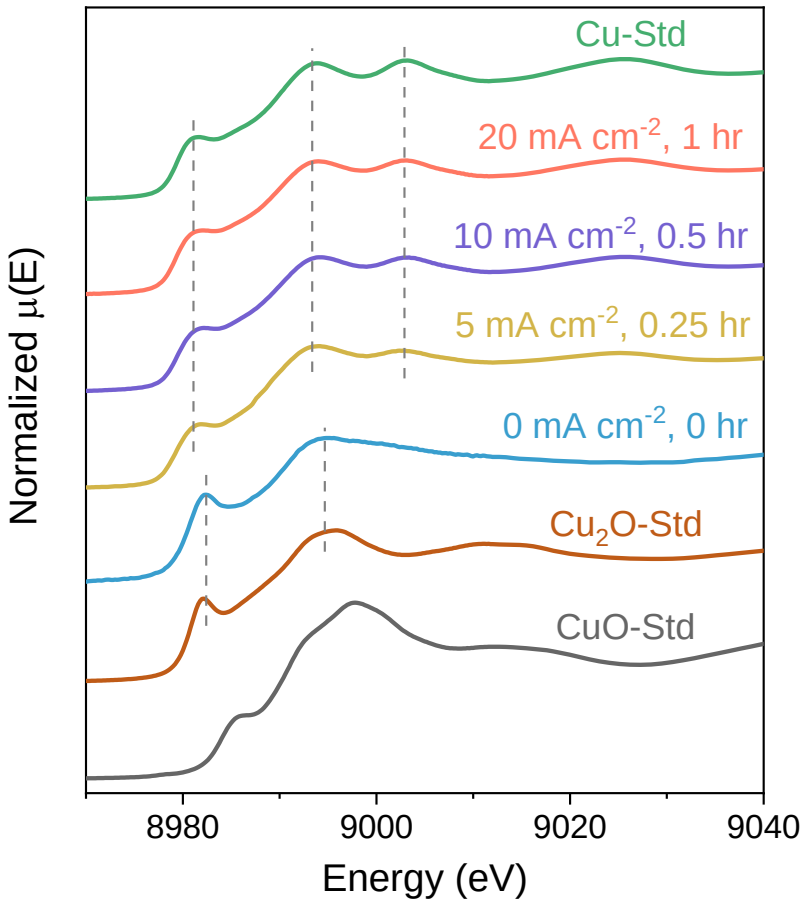

Supplementary Figure 7: *In-situ* X-ray adsorption spectroscopy of a 5 nm thick copper nanosheet catalyst in 5M NH_4OH with 1M KOH.

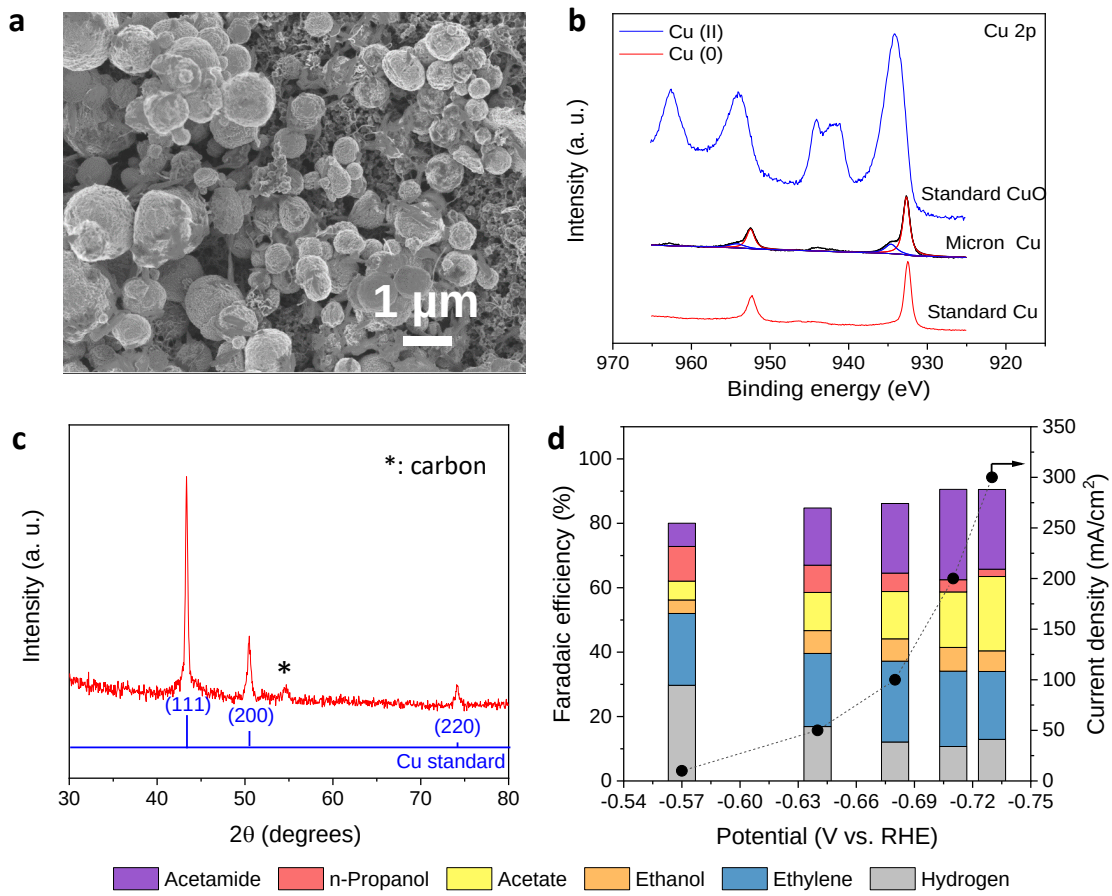

Supplementary Figure 8: Characterization and performance for CO electroreduction with 2:1 (mol/mol) NH_3/CO feed in 1M KOH on micron Cu. a, Scanning electron microscopy image of particles on GDL. **b,** X-ray photoelectron spectroscopy spectra. **c,** X-ray diffraction spectrum. **d,** Current density and Faradaic efficiencies vs. applied potential.

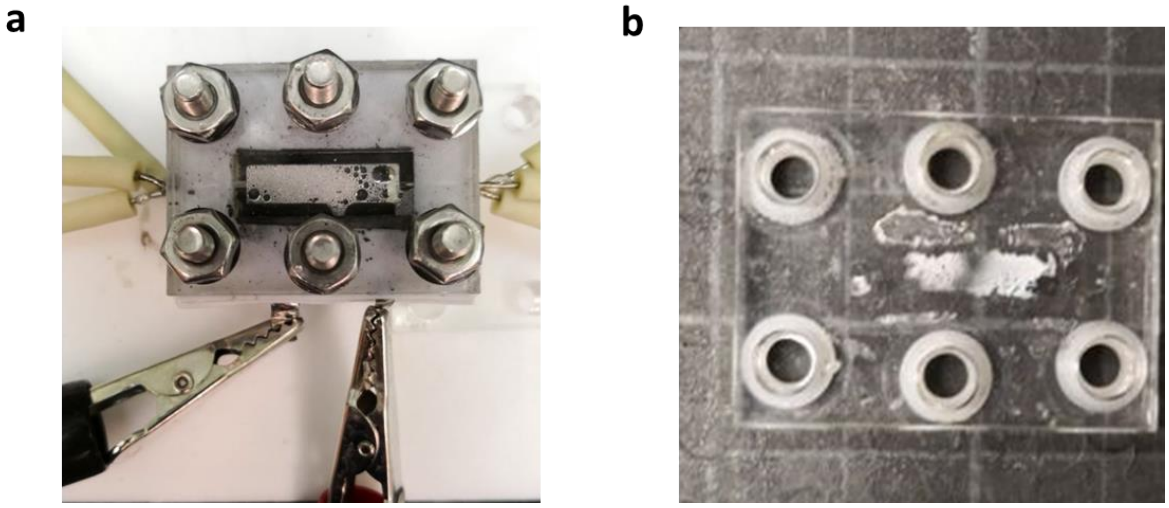

Supplementary Figure 9: (a) Image of flow cell following co-feeding of CO_2 (7 sccm) and NH_3 (15 sccm) with 1M KOH electrolyte showing immediate carbonate formation without applied current and (b) resulting precipitate.

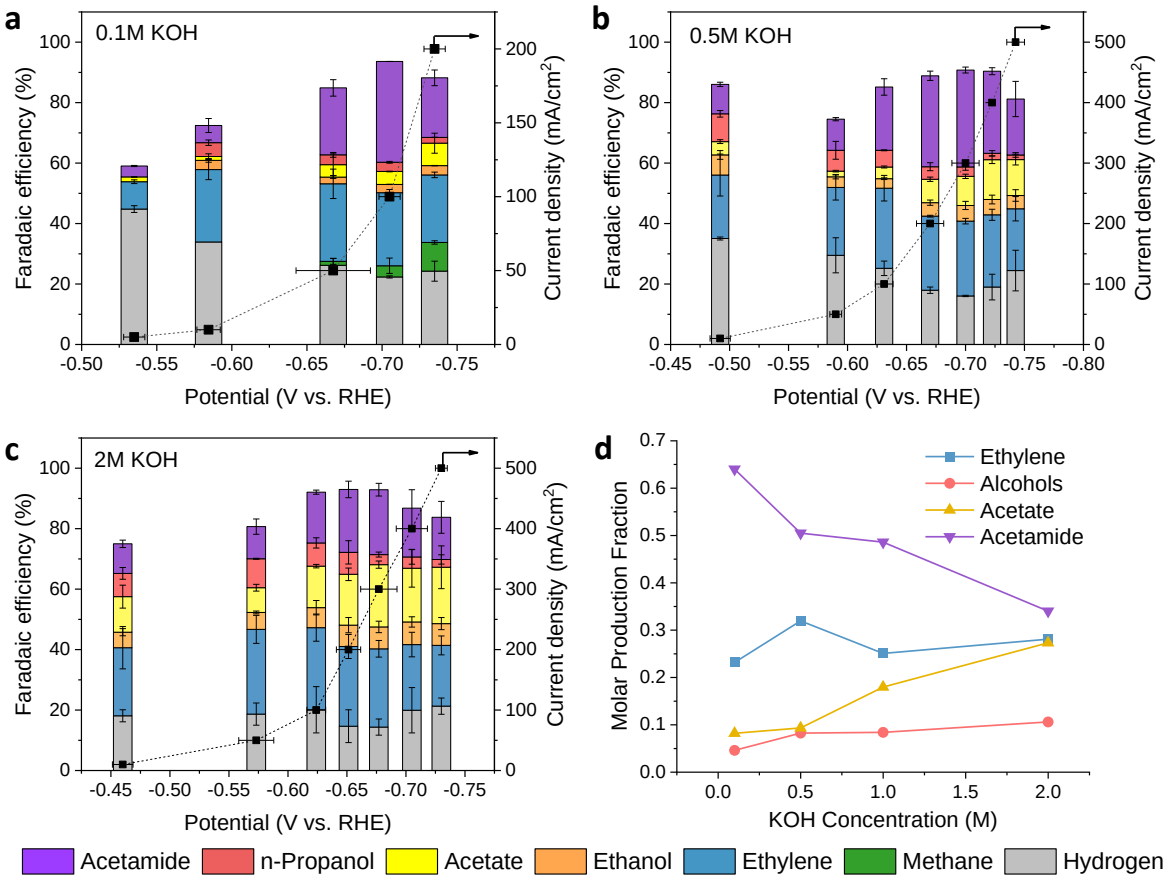

Supplementary Figure 10: CO electroreduction with 2:1 (mol/mol) ammonia to CO ratio in different KOH concentrations. a-c, Current densities and Faradaic efficiencies for 0.1M, 0.5M and 2M KOH. **d,** Molar production fraction of C_{2+} products at 100 mA/cm^2 (excluding hydrogen).

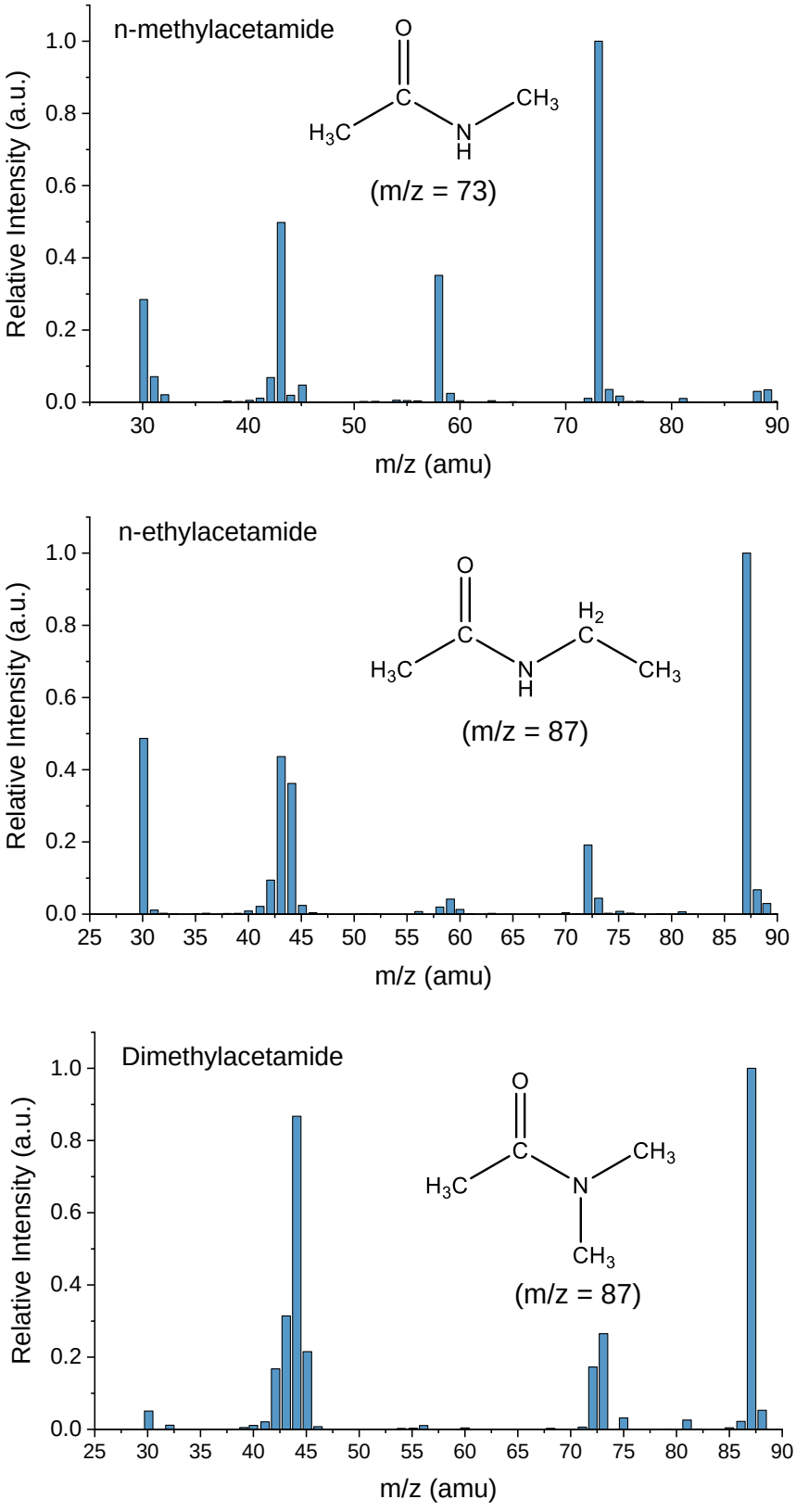

Supplementary Figure 11: Obtained mass spectra for amide products.

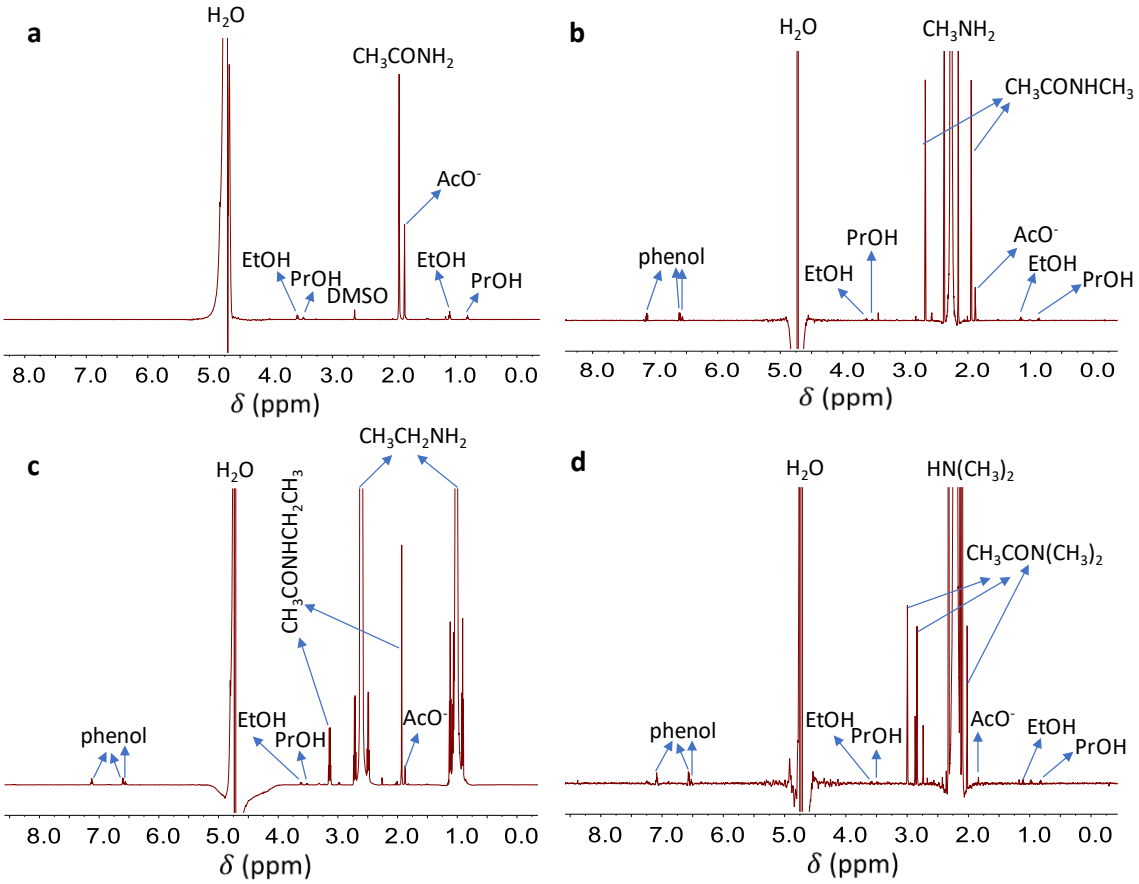

Supplementary Figure 12: Obtained ^{1}H NMR spectra for amide products. a, Acetamide. **b,** N-methylacetamide. **c,** N-ethylacetamide. **d,** N, N-dimethylacetamide.

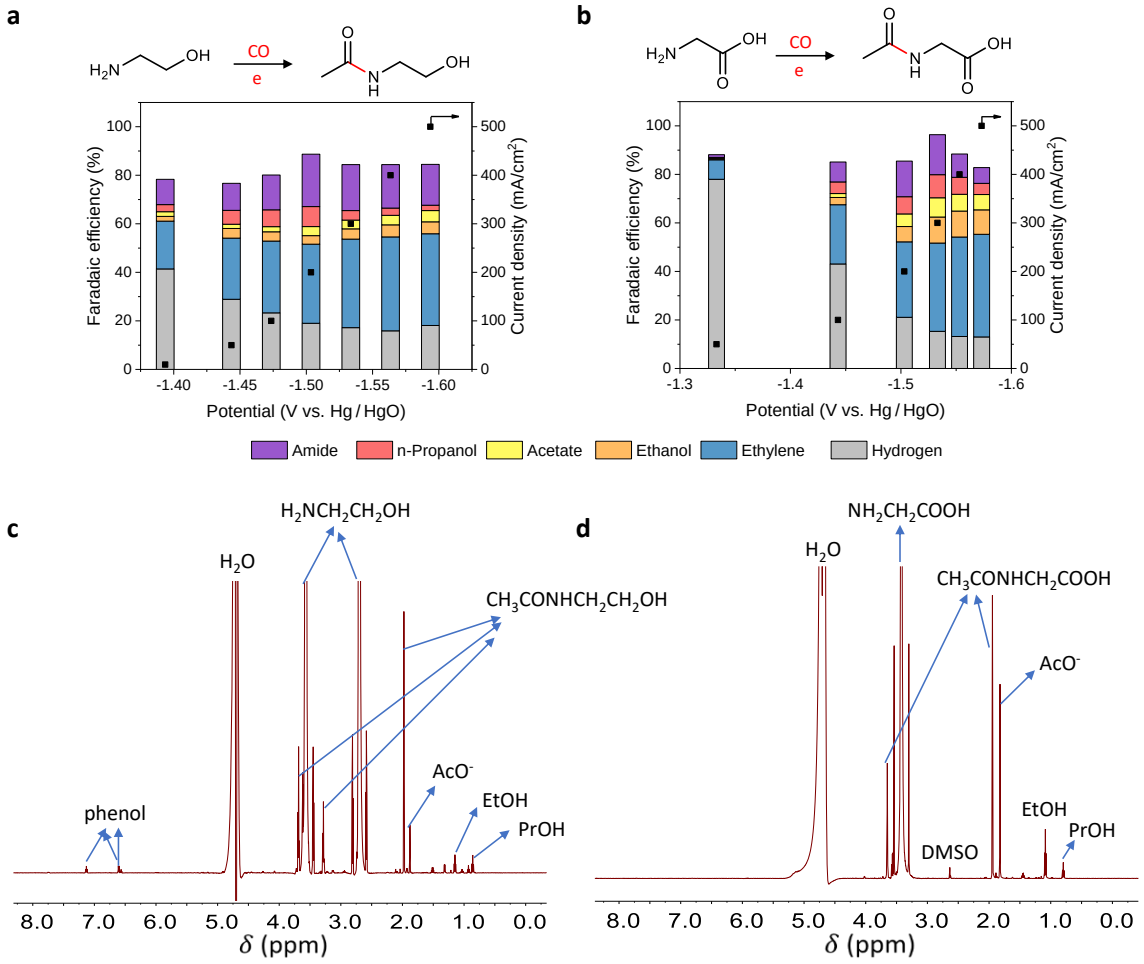

Supplementary Figure 13: Extension to bifunctional amines. a, CO electrolysis data using a 5M solution of ethanolamine with 1M KOH. **b,** CO electrolysis data using a 3M solution of glycine with 1M KOH. **c,** ^{1}H NMR spectrum of acetic monoethanolamide product. **d,** ^{1}H NMR spectrum of aceturic acid product.

Supplementary Table 1: COR (I), COR with NH_3 (II) flow electrolyzer data, and the corresponding stability test data (III) using Cu nanoparticles as the CO reduction catalyst.

I	Electrolyte: 1 M KOH; Flow gas: CO (15 mL/min)						
Potential (V vs. RHE)	Current density (mA cm^{-2})	Faradaic efficiency (%)					
		H_2	C_2H_4	EtOH	AcO^-	PrOH	
-0.45	10	23.4	17.7	4.7	3.0	10.4	
-0.55	50	24.5	23.4	7.8	6.6	11.7	
-0.58	100	19.7	32.8	10.1	11.3	10.9	
-0.62	200	15.9	34.7	13.3	14.4	8.7	
-0.64	300	13.8	37.5	14.0	14.9	7.4	
-0.66	400	12.4	41.0	15.0	15.5	7.1	
-0.69	500	11.8	42.8	14.1	16.3	7.8	
II	Electrolyte: 1 M KOH; Flow gas: CO (7.5 mL/min), NH_3 (15 mL/min)						
Potential (V vs. RHE)	Current density (mA cm^{-2})	Faradaic efficiency (%)					
		H_2	C_2H_4	EtOH	AcO^-	PrOH	CH_3CONH_2
-0.47	10	26.3	17.8	6.2	6.3	8.5	10.0
-0.57	50	20.9	22.8	6.8	4.7	9.9	12.3
-0.63	100	25.0	24.2	4.0	8.7	6.2	23.5
-0.66	200	16.9	22.5	5.4	13.3	4.5	32.7
-0.68	300	14.3	22.9	6.4	17.5	3.6	37.9
-0.7	400	14.9	22.1	6.7	21.1	2.5	34.2
-0.73	500	19.1	19.1	5.5	19.5	1.4	26.3
III	Electrolyte: 1 M KOH; Flow gas: CO (7.5 mL/min), NH_3 (15 mL/min); 100 mA/cm^2						
Potential (V vs. RHE)	Time (h)	Faradaic efficiency (%)					
		H_2	C_2H_4	EtOH	AcO^-	PrOH	CH_3CONH_2
-0.64	1	25.3	28	4.4	13.5	5.8	21.7
-0.64	2	25.9	26.1	3.9	14.8	5.9	21.8
-0.65	3	26.2	25.6	3.8	11.6	4.6	20.3
-0.65	4	26.5	25.1	3.3	12.1	5.0	25.4
-0.66	5	26.9	24.8	4.2	14.9	5.7	25.5
-0.66	6	27.2	24.3	3.4	11.1	3.1	24.1
-0.68	7	27.5	23.9	4.2	11.5	4.3	26.5
-0.70	8	21.8	24.1	4.3	16.4	3.0	25.8

Supplementary Table 2: Flow electrolyzer data for COR with different amino-containing electrolytes using Cu NPs as the CO reduction catalyst.

	Electrolyte: 5 M CH_3NH_2 in 1 M KCl; Flow gas: CO (15 mL/min)						
Potential (V vs. Hg/HgO)	Current density (mA cm^{-2})	Faradaic efficiency (%)					
		H_2	C_2H_4	EtOH	AcO^-	PrOH	$CH_3CONHCH_3$
-1.41	10	30.7	26.2	3.3	1.6	4.9	11.0
-1.50	50	18.9	29.3	2.7	2.2	3.3	28.3
-1.54	100	15.9	27.9	2.9	4.3	4.4	33.2
-1.57	200	14.8	28.5	2.3	5.7	1.5	41.5
-1.59	300	16.6	28.5	2.5	5.6	1.2	37.1
	Electrolyte: 5 M $CH_3CH_2NH_2$ in 1 M KCl; Flow gas: CO (15 mL/min)						
Potential (V vs. Hg/HgO)	Current density (mA cm^{-2})	Faradaic efficiency (%)					
		H_2	C_2H_4	EtOH	AcO^-	PrOH	$CH_3CONHCH_2CH_3$
-1.40	10	36.1	20.2	1.2	4.7	1.4	11.6
-1.49	50	25.1	26.0	4.0	3.6	3.6	19.7
-1.54	100	25.3	27.4	3.2	3.7	2.4	27.1
-1.57	200	28.0	21.5	3.4	3.6	1.6	34.4
-1.59	300	31.0	19.8	2.4	3.4	0.9	29.4
	Electrolyte: 5 M CH_3NHCH_3 in 1 M KCl; Flow gas: CO (15 mL/min)						
Potential (V vs. Hg/HgO)	Current density (mA cm^{-2})	Faradaic efficiency (%)					
		H_2	C_2H_4	EtOH	AcO^-	PrOH	$CH_3CON(CH_3)_2$
-1.34	10	65.8	14.8	0	0	0	4.6
-1.46	50	45.4	21.1	1.8	0	4.1	12.7
-1.49	100	38.0	25.0	0.8	0	2.6	27.4
-1.52	200	36.2	22.9	0.8	0.5	1.6	35.7
-1.55	300	37.8	18.5	2.2	1.1	1.8	34.3

Supplementary Table 3: Electrochemical cathodic reactions for acetamides production through CO electrolysis in various amine precursors

Amine Precursor	Acetamide Product	Electrochemical Reaction
Ammonia	Acetamide	$2CO + NH_3 + 3H_2O + 4e^- \rightarrow CH_3CONH_2 + 4OH^-$
Methylamine	N-Methylacetamide	$2CO + CH_3NH_2 + 3H_2O + 4e^- \rightarrow CH_3CONHCH_3 + 4OH^-$
Ethylamine	N-Ethylacetamide	$2CO + CH_3CH_2NH_2 + 3H_2O + 4e^- \rightarrow CH_3CONHCH_2CH_3 + 4OH^-$
Dimethylamine	N-N-Dimethylacetamide	$2CO + CH_3NHCH_3 + 3H_2O + 4e^- \rightarrow CH_3CONH(CH_3)_2 + 4OH^-$
Ethanolamine	Acetic monoethanolamide	$2CO + NH_2CH_2CH_2OH + 3H_2O + 4e^- \rightarrow CH_3CONHCH_2CH_2OH + 4OH^-$
Glycine	Aceturic Acid	$2CO + NH_2CH_2COOH + 3H_2O + 4e^- \rightarrow CH_3CONHCH_2COOH + 4OH^-$

Simulation Details

We used the PBE-D3 flavor of DFT to predict the reaction processes for the water/Cu(100) interface using 48 explicit water molecules (5 layers, 1.21 nm thick) on a 4×4 Cu (100) surface slab (3 layers) with an area of 1.02 nm^2. We chose Cu(100) as the model surface because Cu(100) is known to be active for CO reduction to multi-carbon products and stable under typical reaction conditions.[1-3] To equilibrate the waters interacting with the interface, we first carried out 2.0 ns of reactive molecular dynamics (RMD) simulations using the ReaxFF reactive force field for Cu and H_2O. Starting from this well-equilibrated interface; we carried out 10 ps of Quantum Mechanic Molecular Dynamics (QM-MD) simulation at 298 K. After that, we used metadynamics and thermodynamic integration to calculate free energy barriers for various reaction steps (the results were averaged over three independent calculations). We find that including one extra Na solvated in the solution leads to a work function of 3.40 (±0.25) eV, which corresponds to -0.59 V at pH = 7 or -0.18V at pH = 14 at RHE scale.

The simulation box is 40 Å along the z-axis with a vacuum of 24 Å. The lateral dimensions of the slab were fixed using the 3.61 Å lattice constant of Cu. Two CO molecules were placed on the 4 × 4 unit cell (on top site) corresponding to a surface coverage of 1/8.

Electronic structure calculations were performed within the DFT framework, as implemented in the Vienna ab initio simulation program (VASP 5.4.4), a plane-wave pseudopotential package, with the projector augmented wave (PAW) method to account for core-valence interactions. We use the PBE flavor of DFT including theD3 empirical correction for London dispersion using Becke-Johnson parameters. The exchange and correlation energies were calculated using the Perdew, Burke, and Ernzerhof (PBE) functional within the generalized gradient approximation (GGA). Spin polarization did not have an appreciable effect on the overall energies. The PBE-D3 method was employed to correct van der Waals interaction of water-water and water-Cu.

We used plane-wave cutoff energy of 400 eV and the First order Methfessel-Paxton scheme with a smearing width of 0.2 eV. Dipole corrections were applied along the z-axis. The Energy minimization criterion was that all forces on free atoms be < 0.02 eV/Å.

We used a 1.0 fs time step in the Molecular Dynamics (MD) simulations. These MD simulations used only the gamma point of the Brillouin zone with no consideration of symmetry. The velocities were rescaled every 20 MD steps to readjust the target temperature to equilibrium. We employed a Nose-Hoover thermostat for the free energy calculations with a temperature damping parameter of 100 fs.

Modeling of pH and Electrolyte

The pH effects are two-fold: first, the applied voltage at SHE scale (U_{SHE}); second, the chemical potential of OH^-. Both effects may have an influence on the prediction of energetic. For the first part, we explicitly considered the effect of pH by converting the work function (or absolution potential, Φ) to RHE scale (U_{RHE}) using the following equation:

$$U_{RHE} = U_{SHE} - 0.0591 \times pH \text{ (where, } U_{SHE} = 4.44 - \Phi) \quad \text{(S1)}$$

For the second part, we assume that the concentration of OH^- has no influence on the transition state, because Markovic et al have demonstrated that H_2O is the proton donator when pH > 3.0.[4] However, OH^- does have an influence on the reaction when OH^- is the product. In these cases, we applied a 0.83 eV to correct the reaction energies.

In our calculations, we always include one Na^+ out of 48 explicit H_2O molecules, corresponding to a concentration of ~1M. We intentionally placed the Na^+ 1 nm away from the surface (the fourth layer) to avoid the adsorption of Na^+ on the electrode surface, and we found that Na^+ stayed at the fourth layer throughout the entire MD simulation. We consider such treatment effectively captures the main features of the effect of non-adsorbed cations, such as K^+ in our experiment. Instead, we consider the difference in the size and cation-water complex structures between Na^+ and K^+ are trivial.

Free Energy Calculations

Enhanced sampling can increase the time scale compared to brute force simulations. We calculated the free energies using metadynamics molecular dynamics (m-MD) and constrained molecular dynamics (c-MD) by defining the collective variables (CVs) of the reactions, which are bond distances (r) for sample reactions or hydrogen bonds (HBs) network when a complex water network is involved in the reaction. The definition of CVs of the investigated reactions is shown in the Supplementary Table 4.

Three parameters are controllable and relevant to the accuracy of a metadynamics simulation: the height of a Gaussian hill (h), the width of the Gaussian hill (ω) and frequency to update the bias potential (t_G). In this work, we chose the parameters of h = 0.08 eV, ω = 0.18 Å and t_G = 24 fs, which allows the desired reaction to complete with simulation times from 2.4 to 9.6 ps as we demonstrated in our previous work.

To increase the statistics, we further selected eleven (11) windows from the reactive trajectories generated from metadynamics simulations to carry out thermodynamic integration calculations. At each window, we took 2 ps simulations to produce the potential of mean force (PMF) by using constraint molecular with the value of CVs fixed, which virtually extend the QM-MD simulation by 2000 times. Finally, free energy profile can be derived by integrating the PMF from blue moon ensemble along with the CVs, which can be used to obtain the free energy barriers (the peak of the profile) and free energy differences. In the Supplementary Figure 14, we show the calculated PMFs (13a) with uncertainties and the free energy profile (13b) of NH_3 addition reaction [*C=C=O + NH_3 → *C=C(OH)NH_2], in which the free energy barrier is distinguished to be 0.51 eV.

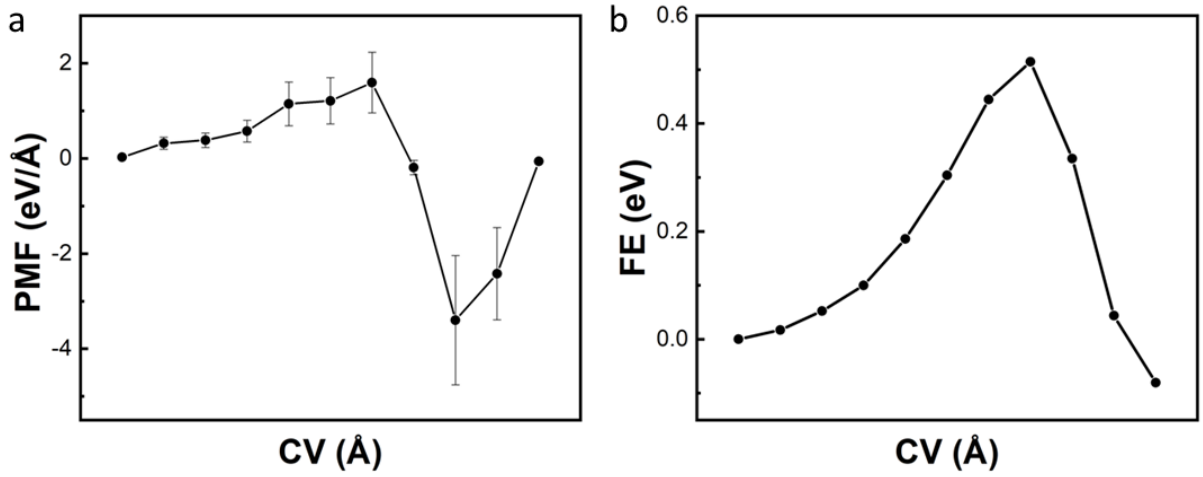

Supplementary Figure 14: (a) The potential of mean force (PMF, in eV/Å) from 2 ps constraint molecular dynamics simulation and (b) the integrated free energy (FE, in eV) profile.

Benchmark of the Influence of Calculation Details to Free Energy Predictions

To make sure that this framework of free energy calculation is sufficient to produce reliable and accurate predictions, we carried benchmark calculations to verify the simulation details including the number of windows and simulation time of PMF calculations:

To estimate the statistics, we increase the number of windows to 15. The free energies predicted from 11 windows and 15 windows are 0.51 eV and 0.57ev, which are comparable considering the uncertainties (0.6 to 0.8 eV) of the calculations as shown in the Supplementary Table 4.

We also tested the influence of sampling time of PMF calculations at 1 ps, 2ps and 3ps. The free energies predicted from 2 ps and 3ps are 0.51 eV and 0.53 eV, which are comparable considering the uncertainties (0.6 to 0.8 eV) of the calculations as shown in the Supplementary Table 4.

Basing on these tests, we consider 11 windows + 2ps simulation represents the best balance of accuracy and computational cost.

The collective variables (CVs) used in the calculations are shown in Table S4. In our calculations, we usually select the hydrogen bonds (HBs) channels to facilitate the proton transfer. However, such CVs added uncertainties in the predictions, because the proton channels depend on the instant configurations of the water network. To test the accuracy, we carried out three calculations starting from the configurations generated from 2ns, 3ns and 4ns reactive force field (ReaxFF) simulations, which can be considered as independent simulations because the correlation time of water molecules at the interface are less than 500 ps. The free energies of these three calculations are 0.57, 0.44 and 0.51 eV, which are comparable considering the uncertainties (0.6 to 0.8 eV) of the calculations as shown in Table Sx. Therefore, we consider CVs defined by HBs are robust, which provide the possibility for accurate predictions.

We also consider the other possibilities of CV definition, such as coordination numbers (CNs). However, the calculation results show that the free energy is overestimated by 0.24 eV as shown in the Supplementary Table 4. Therefore, we consider the HBs is a better descriptor of the reactions, which is also demonstrated to be stable.

Supplementary Table 4: Comparison of the influence of simulation details, which includes the simulation time of reactive force field (ReaxFF) molecular dynamics simulation (in ns), the number of thermodynamic integration (TI) windows (in N), the potential of mean force (PMF) simulation times (in ps), and collective variables (CVs), to the free energies (FE, in eV) without zero-point energy (ZPE) correction.

ReaxFF simulation Time (ns)	**TI windows (N)**	**PMF Simulation Time (ps)**	**CVs**	**FE (eV)**
2	11	1	Hydrogen bonds	0.66±0.8
2	11	2	Hydrogen bonds	0.57±0.7
3	11	2	Hydrogen bonds	0.44±0.8
4	11	2	Hydrogen bonds	0.51±0.6
2	11	2	Coordination numbers	0.75±0.6
2	11	3	Hydrogen bonds	0.54±0.8
2	15	2	Hydrogen bonds	0.57±0.7

Zero-point Energy Corrections

In vacuum QM calculations, zero-point energy (ZPE) can be estimated from a frequency calculation, which is from diagonalizing the hessian second derivative matrix of total energy with respect to atomic coordinates. Such a method has already been implemented in VASP. However, the estimation of ZPE in MD simulation is not that straight-forward. Very recently, we started to employ the two-phase thermodynamic (2PT) model to extract entropies and quantum effect.[5] This combination of MD and 2PT analysis allows us to estimate the contributions from ZPE. The predicted free energies with and without ZPE are shown in Supplementary Table 5. Note that the values with ZPE are used in Figure 2.

Supplementary Table 5: The predicted free energy barriers ($\Delta G^{\ddagger}$) and free energy differences (ΔG) with and without zero-point (ZPE) energy corrections (The ZPE corrections are derived from 2PT analysis taking the QM-MD trajectory as input).

Reactions	CV	$\Delta G^{\ddagger}$(eV)	$\Delta G^{\ddagger}$+ZPE(eV)	ΔG(eV)	ΔG +ZPE(eV)
*(HO)C=COH + e^-→*C=COH + OH^-	r_{OH}	0.62	0.61	0.03	0.01
*(HO)C=COH→*C=C=O + H_2O	HBs	0.59	0.57	-0.23	-0.26
*C=C=O + NH_3→*C=C(OH)NH_2	HBs	0.51	0.53	-0.08	-0.06
*C=C=O + NH_3→*C=C(OH)NH_2 (with K^+)	HBs	0.52	-	-	-
*C=C=O + H_2O→*C=C(OH)OH	HBs	0.88	0.89	0.41	0.40
*C=C=O + OH^-→*C=C(OH)O^-	HBs	0.71	0.72	0.29	0.28
*C=C(OH)NH_2→*CH-C(O)NH_2	HBs	-	-	-0.12	-0.11
*C=C(OH)OH→*CH-C(O)OH	HBs	-	-	0.36	0.38
*C=C(OH)O^-→*CH-C(O)O^-	HBs	-	-	0.27	0.29

Prediction of Hydrogen Evolution Reaction (HER)

In our calculations, we predicted the free energy barrier and free energy difference of Volmer reaction is 0.81 eV and 0.55 eV. We predicted the free energy barrier of Heyrovsky reaction is 0.89 eV. Taking these energies as an input of the kinetic model, we predict the current density as shown in the Supplementary Figure 15, from which we estimated an overpotential of HER of ~0.4 V, consistent with the experiment.[6]

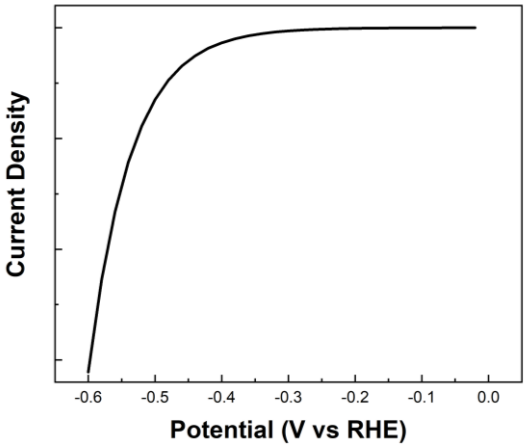

Supplementary Figure 15: The current density of HER predicted from the kinetic model.[7]

Supplementary References:

1. Y.-G. Kim, J. H. Baricuatro, A. Javier, J. M. Gregoire, M. P. Soriaga, The Evolution of the Polycrystalline Copper Surface, First to Cu(111) and Then to Cu(100), at a Fixed CO_2RR Potential: A Study by Operando EC-STM. *Langmuir* **30**, 15053-15056 (2014).

2. K. J. Schouten, Z. Qin, E. Perez Gallent, M. T. Koper, Two pathways for the formation of ethylene in CO reduction on single-crystal copper electrodes. *J Am Chem Soc* **134**, 9864-9867 (2012).

3. Y. Huang, A. D. Handoko, P. Hirunsit, B. S. Yeo, Electrochemical Reduction of CO_2 Using Copper Single-Crystal Surfaces: Effects of CO* Coverage on the Selective Formation of Ethylene. *ACS Catalysis* **7**, 1749-1756 (2017).

4. Strmcnik, D., Lopes, P. P., Genorio, B., Stamenkovic, V. R. & Markovic, N. M. Design principles for hydrogen evolution reaction catalyst materials. Nano Energy 29, 29-36, (2016).

5. Cheng, T., Fortunelli, A. & Goddard, W. A. Reaction intermediates during operando electrocatalysis identified from full solvent quantum mechanics molecular dynamics. PNAS (2019). doi:10.1073/pnas.1821709116.

6. Luc, W., Jiang, Z., Chen, J. G. G. & Jiao, F. Role of Surface Oxophilicity in Copper-Catalyzed Water Dissociation. *ACS Catal.* **8**, 9327-9333, (2018).

7. Exner, K. S.; Sohrabnejad-Eskan, I.; Over, H., *ACS Catal.* **8**, 1864-1879, (2018).